Nano Research 2015, 8(12): 3944–3953
DOI 10.1007/s12274-015-0895-7
Research Article
ISSN 1998-0124
CN 11-5974/O4

Remarkable anisotropic phonon response in uniaxially strained few-layer black phosphorus

Yanlong Wang[1,§], Chunxiao Cong[1,§], Ruixiang Fei[2], Weihuang Yang[1], Yu Chen[1], Bingchen Cao[1], Li Yang[2] (✉), and Ting Yu[1,3] (✉)

[1] *Division of Physics and Applied Physics, School of Physical and Mathematical Sciences, Nanyang Technological University, 637371, Singapore*
[2] *Department of Physics, Washington University in St. Louis, St. Louis, Missouri 63130, USA*
[3] *Department of Physics, Faculty of Science, National University of Singapore, 117542, Singapore*
[§] *These authors contributed equally to this work.*

Received: 21 July 2015
Revised: 6 September 2015
Accepted: 8 September 2015

KEYWORDS
black phosphorus,
uniaxial strain,
Raman spectroscopy,
anisotropy,
density functional theory

ABSTRACT

Black phosphorus (BP) is a good candidate for studying strain effects on two-dimensional (2D) materials beyond graphene and transition-metal dichalcogenides. This is because of its particular ability to sustain high strain and remarkably anisotropic mechanical properties resulting from its unique puckered structure. We here investigate the dependence of lattice vibrational frequencies on crystallographic orientations in uniaxially strained few-layer BP by *in-situ* strained Raman spectroscopy. The out-of-plane A_g^1 mode is sensitive to uniaxial strain along the near-armchair direction whereas the in-plane B_{2g} and A_g^2 modes are sensitive to strain in the near-zigzag direction. For uniaxial strains applied away from these directions, all three phonon modes are linearly redshifted. Our experimental observation is explained by the anisotropic influence of uniaxial tensile strain on structural properties of BP using density functional theory. This study demonstrates the possibility of selective tuning of in-plane and out-of-plane phonon modes in BP by uniaxial strain and makes strain engineering a promising avenue for extensively modulating the optical and mechanical properties of 2D materials.

1 Introduction

Two-dimensional (2D) materials, such as graphene and transition metal dichalcogenides (TMDs), have attracted much attention in recent years for their remarkable properties [1–6]. However, despite their high mobility, graphene-based transistors have an unsatisfactory on/off ratio due to the absence of an intrinsic band gap [7, 8]. On the other hand, TMD materials have a low mobility despite having a high

Address correspondence to Ting Yu, yuting@ntu.edu.sg; Li Yang, lyang@physics.wustl.edu

on/off ratio [9, 10]. The search for alternative 2D materials has thus generated interest in black phosphorus (BP), that has been revisited from the perspective of an atomically thin material. BP, the most stable allotrope of phosphorus, possesses a direct band gap, regardless of thickness, that is tunable from 2.15 eV in a monolayer to the bulk value of 0.3 eV [11]. This range spans intermediate values between graphene and TMDs, making BP appropriate for near- and mid-infrared optoelectronics [12]. Moreover, the combination of on/off ratio and mobility in BP provides conditions that are unattainable with either graphene or TMDs. Finally, its unique puckered structure produces many interesting anisotropic electrical [13, 14], optical [13, 15, 16], thermal [17, 18], and mechanical [19–22] properties.

Strain serves as an effective handle for tuning the properties of 2D materials. Many investigations on graphene showed that lattice vibrations [23–26], electronic band structure [27], and magnetism [28] could be significantly influenced by strain. In addition to being used for phonon softening or determining crystallographic orientation [29–31], strain effects on TMDs have been extended to light-emission tuning via, e.g., a linear band gap redshift [30, 32, 33], a direct-to-indirect band gap transition [30], an enormous valley drift [34], and decreased valley polarization [35]. Because of its ability to sustain a high strain (30% for monolayer BP and 32% for a few layers) [22], BP is considered a good candidate for further studying strain effects on 2D materials. More importantly, its unique puckered structure could yield a remarkably anisotropic mechanical response [19–22], in stark contrast to the crystal-orientation-independent effects of uniaxial strain in both graphene and TMD materials [25, 33, 35, 36]. Various interesting properties of strained BP have been predicted theoretically, such as a negative Poisson ratio [21], a direct-to-indirect band gap transition [37], a rotation of the preferred conducting direction [38], and a semiconductor-to-metal transition [39]. However, to the best of our knowledge, an experimental study of strain-dependent phonon properties in BP remains to be done. An experimental investigation of the strain dependence of BP properties should benefit the development of BP-based flexible electronics.

Here, we report the remarkable dependence of phonon behavior on crystallographic orientations in uniaxially strained few-layer BP. We focus on few-layer BP samples of thickness 4–10 nm, as this range may offer the best compromise between the on/off ratio and mobility [12]. The anisotropic response of lattice vibrational frequencies to uniaxial strain was clearly revealed by Raman spectroscopy. We found that strain in the near-armchair direction can soften the out-of-plane A_g^1 mode while keep the two in-plane phonon modes nearly unchanged. When the tensile strain is applied approximately along the zigzag direction, there is a linear redshift in the B_{2g} and A_g^2 modes, with no change in the A_g^1 mode. This direction-dependent phonon behavior under uniaxial strain in few-layer BP can be explained in terms of the anisotropic influence of tensile strain on structural parameters of BP using density functional theory (DFT). Our work not only confirms the anisotropic optical and mechanical properties of BP experimentally, but also provides a reference for quantifying strain and estimating its orientation by Raman spectroscopy.

2 Experimental

Thin BP layers were fabricated by mechanical exfoliation onto polyethylene terephthalate (PET) substrates, and *in-situ* strained Raman measurements were performed after determining the crystal orientation. Atomic-force microscopy (AFM) measurements were then performed to determine the sample thicknesses.

Sample preparation: BP samples were obtained by micromechanical cleavage [40] of a bulk BP crystal (HQ Graphene, CAS #7803-51-2, Netherlands) and transferred onto PET substrates. Flakes suitable for further study were identified using an optical microscope (Olympus BX 51).

Characterization: Polarization-dependent Raman measurements were performed on the BP samples immediately after they were fixed onto the strain stage to identify their crystal orientations. In our parallel polar configuration, a half-wave plate was used to obtain different linear polarizations of the incident light; a linear polarizer was used to collect the scattered light with a polarization parallel to that of the incident beam. The samples were then stored in a vacuum chamber to minimize natural degradation. Once the samples were firmly bound to the strain stage (generally after

~10 hours), *in-situ* strained Raman measurements were conducted as described previously [30]. All the Raman spectra were taken in the back-scattering configuration by a WITec CRM200 Confocal Raman system with 2400 and 1800 lines·mm^{-1} gratings under 532 nm laser excitation. The laser-spot diameter was estimated to be ~500 nm. The laser power at the sample surface was carefully maintained below 0.2 mW to avoid laser-induced damage. The Raman measurements were conducted under the same conditions for the different strains. Tapping-mode AFM (Veeco, Nanoscope V) was used to determine the thickness. The BP samples were transferred between the different measurement systems in a vacuum container (Circular Bottom Desi-Vac, Fisher Scientific) with a built-in manual vacuum pump. All the measurements were conducted at room temperature.

3 Calculation methods

The atomic structure of the few-layer BP systems was fully relaxed, according to the forces and stresses calculated by DFT within the local density approximation (LDA). All atoms were allowed to relax until the residual force per atom converged to within 0.001 eV·Å^{-1}. Electronic structures were obtained by solving the Kohn–Sham equation with norm-conserving pseudopotentials. A 14 × 10 × 1 *k*-point sampling grid was chosen and 35 Ry was used as the plane-wave cutoff energy for the convergence calculations.

4 Results and discussion

As mentioned above, the unique puckered structure characteristic of orthorhombic BP is clearly seen in Fig. 1(a). Each unit layer consists of covalently bonded phosphorus atoms from two sub-planes, which form a hinge-like structure [41]. The *x* axis is defined as the zigzag direction along the ridge orientation, and the *z* axis denotes the armchair direction parallel to the hinge direction. Along the out-of-plane *y* direction, layers are held in a Bernal (AB) stacking sequence by van der Waals force. As can be seen from the top view in Fig. 1(b), unlike graphene, BP exhibits a hexagonal structure in the *x*–*z* plane, comprising two kinds of edges with significantly different lengths [12]. Bulk BP belongs to the point group D_{2h}^{18} (mmm) and the space group *Cmce* [42]. It displays twelve phonon modes at the Γ point in the Brillouin zone, six of which are Raman active [42, 43]. In the normal backscattering configuration, only the A_g (containing both A_g^1 and A_g^2) and B_{2g} modes have a non-zero Raman scattering intensity [15, 16]. Figure 1(c) shows the typical Raman spectrum of BP on a PET substrate (the corresponding optical image is shown in Fig. 3(c)). It reveals three distinct bands at 361, 438, and 467 cm^{-1}, which are attributed to the A_g^1, B_{2g}, and A_g^2 modes, respectively [15]. The symmetry classification of Raman modes and the corresponding Raman tensors apply to BP regardless of thickness, because thin layers (either odd- or even-numbered) share the same point group (D_{2h}) as the bulk [42]. The atomic displacements of the three phonon modes are plotted in Fig. 1(d) [15, 16, 43]. A_g^1 is an out-of-plane mode, with the phosphorus atoms in the top and bottom sublayers vibrating in opposite directions. In contrast, the B_{2g} and A_g^2 modes involve in-plane zigzag and armchair oscillations, respectively, with adjacent atoms vibrating out of phase. Figures S1(a) and S1(b) in the Electronic Supplementary Material (ESM) show AFM images of the few-layer BP flakes 1 and 2 studied

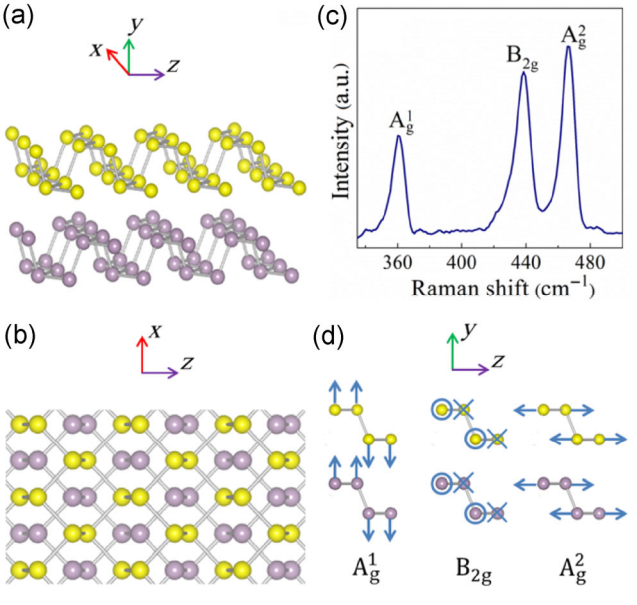

Figure 1 (a) Perspective and (b) top views of two layer (2L) BP with a puckered structure. Yellow and gray are used to distinguish the top and bottom layers, respectively. (c) Typical Raman spectra of BP on PET. (d) Schematic diagram of atomic displacements in the observed phonon modes.

in this work (corresponding optical images are shown in Figs. 2(c) and 3(c)). The thicknesses of flakes 1 and 2 are 5.5 and 10.4 nm, respectively, corresponding to an estimated 9 and 17 layers.

Raman spectroscopy is an effective and nondestructive tool for investigating the number of layers [44–47], influence of stacking [48–51], edge chirality [52–54], optical conductivity [55], and thermal effects [56–60] in graphene and TMD materials. It has recently also been applied to 2D BP [15, 16, 42, 43, 61–65]. Here, we identified the crystal orientations of our BP samples using polarization-dependent Raman spectroscopy before applying strain [15, 16, 42]. The parallel polar configuration for the polarization-dependent Raman measurements is schematically illustrated in Fig. S2 in the ESM. The incident and scattered polarizations were kept parallel and rotated simultaneously with a step size of 30°. Assuming that the zigzag direction of the BP sample forms an angle θ relative to the horizontal direction, and that both the incident and scattered polarizations are rotated to a position where they form an angle φ with the horizontal, we obtain the following expressions for the intensities of the three phonon modes, based on their Raman tensors and the polarization vectors (see detailed discussion in the ESM) [16]

$$I_{A_g^1} \propto [|a_1| \cos^2(\varphi - \theta) + |c_1| \sin^2(\varphi - \theta)]^2 \quad (1)$$

$$I_{B_{2g}} \propto [|e| \sin(2\varphi - 2\theta)]^2 \quad (2)$$

$$I_{A_g^2} \propto [|a_2|^2 \cos^4(\varphi - \theta) + |c_2|^2 \sin^4(\varphi - \theta)] \quad (3)$$

Polarization-dependent Raman spectroscopy was performed after mounting the sample onto the strain stage to accurately determine the relative angle between its crystal orientation and the strain direction (fixed along the horizontal direction). Figure S3(a) in the ESM shows the Raman spectra as functions of the polar angle for flake 1. When the polarization is rotated from 0° to 180°, the A_g^1 mode intensity does not change significantly while those of the B_{2g} and A_g^2 modes are very sensitive. Lorentzian functions were chosen to fit the obtained Raman spectra; the polarization-dependent phonon intensities plotted in Figs. S3(b)–S3(d) in the ESM are well fitted by Eqs. (1), (2), and (3), respectively. Specifically, the B_{2g} mode intensity has

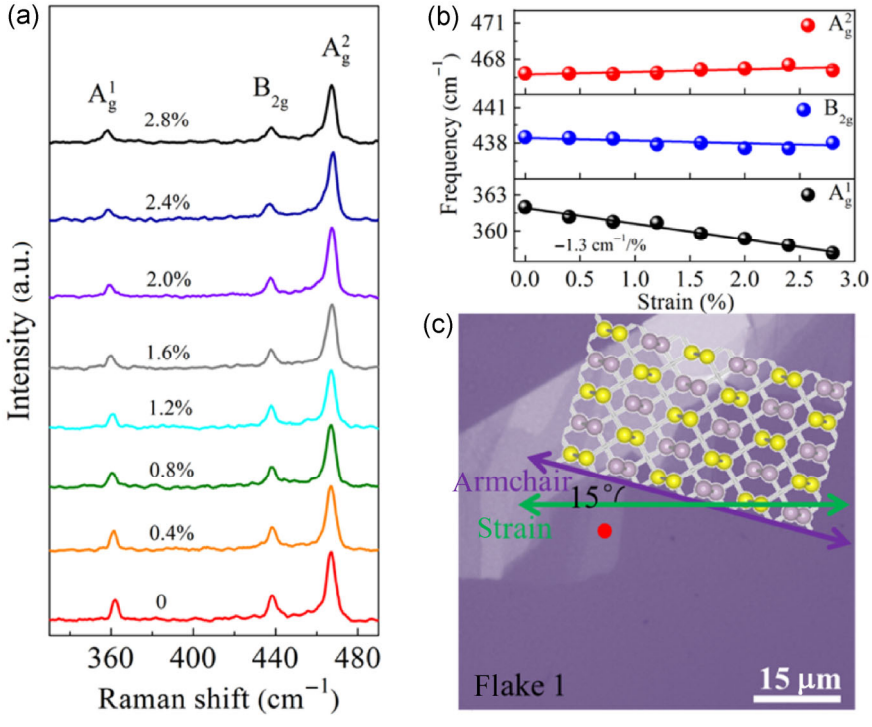

Figure 2 (a) Raman spectra and (b) fitted phonon frequencies as functions of uniaxial strain for flake 1. The relationship between the armchair orientation and uniaxial strain direction is shown in (c). The red point indicates the position where strain-dependent Raman spectra were taken.

a variation period of 90°, with the two minimum-intensity angles (75° and 165°) corresponding to the armchair and zigzag directions. On the other hand, the two A_g mode intensities vary with a period of 180°, reaching maxima when the polarization is along the armchair direction (φ = 165°) and becoming weaker when the polarization angle is further rotated by 90° (φ = 75°). In addition, the more remarkable sensitivity of the A_g^2 mode to the polarization angle, compared with that of the A_g^1 mode, is due to the distinctive c/a ratios for these two modes, where a and c are the Raman tensor elements in Eqs. (1) and (3). All three fitted curves in Figs. S3(b)–S3(d) simultaneously give θ = 75°, which indicates that the armchair direction forms an angle of 15° with the strain orientation. The *in-situ* strained Raman measurements were next performed. Figure 2(a) shows the evolution of the Raman spectra in flake 1 as functions of the uniaxial strain. As the strain increases from 0 to 2.2%, there is a clear redshift in the A_g^1 mode whereas the two in-plane modes are insensitive to strain. As can be seen in the fitted lattice vibrational frequencies versus strain (Fig. 2(b)), the A_g^1 mode is linearly redshifted at a rate of –1.3 cm^{-1}/% while the shift rates of B_{2g} and A_g^2 modes are negligible when tensile strain is applied near the armchair direction.

To probe the crystal-orientation-dependent effects of uniaxial strain in BP further, we then studied the evolution of lattice vibrations under strain in the zigzag direction. The same method was applied to identify the crystal orientation of flake 2 after it was fixed onto the strain stage. Polarization-dependent Raman spectra are plotted in Fig. S3(e) in the ESM. In contrast to flake 1, the maximum intensities of the A_g and B_{2g} modes in flake 2 appear at 100° and 55° (145°), respectively. By fitting the phonon intensities as functions of φ (Figs. S3(f)–S3(h) in the ESM), we obtained θ = 10° for flake 2, which shows that the zigzag direction in flake 2 is very close to the strain direction, as indicated in Fig. 3(c). The strain-dependent Raman spectra of flake 2 are shown in Fig. 3(a). To demonstrate the evolution of phonon frequencies under strain precisely, the frequencies of the three phonon peaks, plotted as functions of strain, were estimated from Lorentzian fits and plotted in Fig. 3(b). Contrary to the observations in the near-armchair

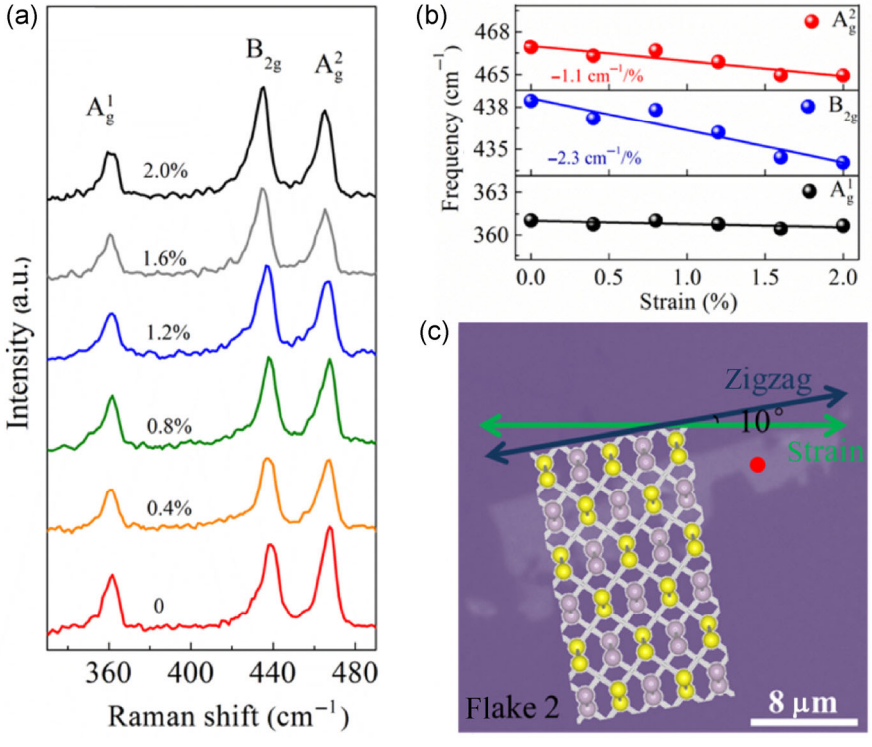

Figure 3 (a) Raman spectra and (b) fitted phonon frequencies as functions of uniaxial strain for flake 2. The relationship between the zigzag and uniaxial-strain directions is shown in (c). The red point indicates the position where strain-dependent Raman spectra were taken.

strain direction, the B_{2g} and A_g^2 modes are linearly redshifted with the tensile zigzag strain (at rates of –2.3 m^{-1}/% and –1.1 cm^{-1}/%, respectively), whereas the A_g^1 mode is unaffected. For a specific vibrational mode under strain, the relative change in the force constant relative to the unstrained value is approximately $\frac{\Delta k}{k} \simeq 2\frac{\Delta\omega}{\omega}$, where ω and $\Delta\omega$ are the unstrained vibrational frequency and the change in vibrational frequency due to strain, respectively. Hence, the force constant is insensitive to uniaxial strain because ω is usually much greater than $\Delta\omega$ for small strains. For example, under our applied armchair and zigzag strains of 2%, we estimate the relative change in the force constant to be only approximately 1.4% and 0.1%, respectively, for the A_g^1 mode.

To better understand the observed remarkable dependence of phonon behavior on crystallographic orientation in uniaxially strained few-layer BP, we calculated the evolution of the geometric properties, under both armchair and zigzag strains (0–3%), in BL comprising two, three (3L), four (4L), or five (5L) layers.

Important physical parameters are marked in the top (Fig. 4(a)) and side views (Fig. 4(b)), e.g., the two inequivalent bond lengths (in-plane r_1 and out-of-plane r_2) and the inter-layer gap L, the shortest distance between two phosphorous atoms in the neighboring layers. Figure 4(c) shows the response of the structural parameters to both armchair (ε_z) and zigzag (ε_x) strains for 5L BP, and Fig. S4 in the ESM shows those for 2L to 4L BP. A linear dependence is observed in all cases within the range of 0 to 3% strain. The calculated parameters of the unstrained few-layer BP, including the inter-layer gap, bond lengths, and bond angles (results not shown here) are in good agreement with previous theoretical calculations [14, 20, 39]. Because the variations in the structural parameters are qualitatively similar for 2L to 5L BP, we shall consider the 5L BP (for which the thickness is closer to that of our measured samples) to explain the strained Raman results. Table 1 summarizes the slopes of r_1, r_2, and L versus the armchair and zigzag strains for 2L to 5L BP, obtained from linear fits. The schematic diagram (Fig. 1(d)) of atomic displacements in the A_g^1 mode show that the restoring force acting on a given atom is mainly exerted by its nearest neighbors in both the

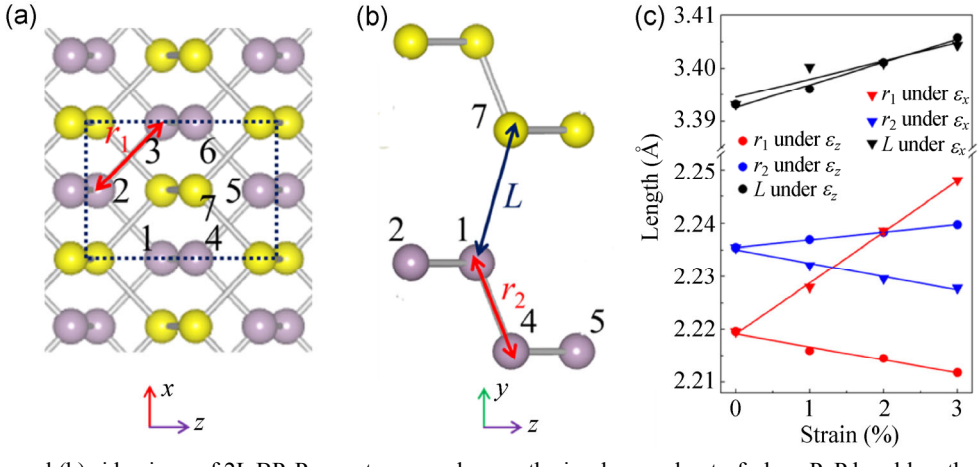

Figure 4 (a) Top and (b) side views of 2L BP. Parameters r_1 and r_2 are the in-plane and out-of-plane P–P bond lengths, respectively. L is the inter-layer distance. The unit cell is indicated with the blue dashed rectangle. (c) Calculated values for r_1, r_2, and L, as functions of uniaxial strain along the armchair and zigzag directions in 5L BP.

Table 1 Linearly fitted slopes of r_1, r_2, and L (Å/%) versus armchair and zigzag strains for 2L to 5L BP

Strain direction	2L			3L			4L			5L		
	r_1 (Å/%)	r_2 (Å/%)	L (Å/%)	r_1 (Å/%)	r_2 (Å/%)	L (Å/%)	r_1 (Å/%)	r_2 (Å/%)	L (Å/%)	r_1 (Å/%)	r_2 (Å/%)	L (Å/%)
Armchair	−0.0005	0.0013	0.0085	−0.0022	0.0020	0.0044	−0.0015	0.0018	0.0056	−0.0025	0.0014	0.0043
Zigzag	0.0087	−0.0020	0.0013	0.0090	−0.0026	0.0026	0.0091	−0.0027	0.0041	0.0096	−0.0026	0.0035

adjacent layer and neighboring sublayer in the same layer, which vibrate out of phase with it. Consider atom 1 for example. Its interactions with atoms 4 and 7 force it back to its equilibrium position during out-of-plane oscillation, and therefore r_2 and L significantly influence the vibrational frequency of the A_g^1 mode. When under strain in the armchair direction, r_2 and L both increase, lowering the restoring force and resulting in a redshift of the A_g^1 mode. In contrast, strain along the zigzag direction increases L while reducing r_2 at similar rates. Consequently, the overall restoring force varies little and the A_g^1 mode is insensitive to zigzag strain. With regard to the B_{2g} and A_g^2 phonon modes, all three nearest atoms influence the in-plane vibrational frequencies of a given atom, which can be seen from the schematic representation shown in Fig. 1(d). The three parameters r_1, r_2, and L must therefore be considered simultaneously when analyzing the trends of these two modes under strain. When strain is applied in the armchair direction, r_1 decreases while r_2 and L increase. Though the slope of L is somewhat greater than that of the other two parameters, the change in L under a given strain relative to its unstrained value is in fact similar to the change in r_1, owing to the larger value of L in pristine BP. As a result, the effects of changing these three parameters on lattice vibrations under strain in the armchair direction are roughly offset due to their opposite effects with similar strength so that no clear shift of the B_{2g} or A_g^2 mode is observed. On the other hand, in the case of strain in the zigzag direction, our calculations suggest an increase in r_1 and L and a slight reduction in r_2. Because of the higher rate of change in r_1 compared with the other two parameters (by factors 3.7 and 2.7 for r_2 and L, respectively), the overall restoring force is weakened under zigzag strain and leads to a softening of the B_{2g} and A_g^2 modes. As seen in Fig. 4(a), the bond between atoms 1 and 4 is perpendicular to the zigzag direction in the unstrained BP structure, and therefore the corresponding covalent force makes a trivial contribution to the restoring force in the B_{2g} mode. Accordingly, the decrease in this bond length r_2 barely influences the frequency of B_{2g} as it does that of the A_g^2 mode. This explains why the shift in frequency due to strain in B_{2g} is greater than that in A_g^2.

Finally, to gain a comprehensive view of the anisotropic response of lattice vibrations to uniaxial strain in BP, we explored the effects of uniaxial strain between the aforementioned extreme conditions. Using the method described above, we measured $\theta = -56°$ for flake 3 from 2D polar maps (data not shown). In this case, strain was applied at 34° relative to the armchair direction (Fig. S5(c) in the ESM). Under this strained condition, a detectable softening occurs for all three phonon modes (see Fig. S5(a) in the ESM). As shown in Fig. S5(b) in the ESM, the linear redshift rates are extrapolated to give –1.1, –1.4, and –0.5 m^{-1}/% for the A_g^1, B_{2g}, and A_g^2 modes, respectively.

5 Conclusions

We have identified different crystal orientations in few-layer BP flakes on a flexible substrate and investigated the distinct responses of their lattice vibrations to adjustable uniaxial tensile strain. We demonstrated that the out-of-plane A_g^1 mode is sensitive to uniaxial strain along the near-armchair direction, whereas the in-plane B_{2g} and A_g^2 modes are sensitive to near-zigzag direction strain. When the strain is applied in intermediate directions, all three phonon modes are linearly redshifted. Our DFT calculations clearly demonstrate the anisotropic mechanical response to uniaxial strain in BP as a consequence of its unique puckered crystal structure. They could be used to elucidate the striking dependence of strained phonon frequencies on crystal orientations. Our findings extend previous studies on strained atomically thin layered materials, giving a better understanding of rich strain-engineered phonon modifications in 2D materials. The special anisotropic response of lattice vibrations to strain makes BP promising for diverse applications, such as for detecting strain orientation.

Acknowledgements

This work is supported by MOE Tier 2 (No. MOE2012-T2-2-049) and MOE Tier 1 (No. MOE2013-T1-2-235). R. X. Fei and L. Yang acknowledge support from the National Science Foundation (NSF) (No. DMR-1207141) and NSF CAREER (No. DMR-1455346).

Electronic Supplementary Material: Supplementary

material (polarization dependence of phonon modes, AFM images, polarization geometry, calculated structural parameters of strained BP, and phonon response in uniaxially strained BP flake 3) is available in the online version of this article at http://dx.doi.org/10.1007/s12274-015-0895-7.

References

[1] Novoselov, K. S.; Geim, A. K.; Morozov, S. V.; Jiang, D.; Katsnelson, M. I.; Grigorieva, I. V.; Dubonos, S. V.; Firsov, A. A. Two-dimensional gas of massless Dirac fermions in graphene. *Nature* **2005**, *438*, 197–200.

[2] Castro Neto, A. H.; Guinea, F.; Peres, N. M. R.; Novoselov, K. S.; Geim, A. K. The electronic properties of graphene. *Rev. Mod. Phys.* **2009**, *81*, 109–162.

[3] Cong, C. X.; Shang, J. Z.; Wu, X.; Cao, B. C.; Peimyoo, N.; Qiu, C. Y.; Sun, L. T.; Yu, T. Synthesis and optical properties of large-area single-crystalline 2D semiconductor WS_2 monolayer from chemical vapor deposition. *Adv. Opt. Mater.* **2014**, *2*, 131–136.

[4] Peimyoo, N.; Shang, J. Z.; Cong, C. X.; Shen, X. N.; Wu, X. Y.; Yeow, E. K. L.; Yu, T. Nonblinking, intense two-dimensional light emitter: Monolayer WS_2 triangles. *ACS Nano* **2013**, *7*, 10985–10994.

[5] Cooper, R. C.; Lee, C.; Marianetti, C. A.; Wei, X. D.; Hone, J.; Kysar, J. W. Nonlinear elastic behavior of two-dimensional molybdenum disulfide. *Phys. Rev. B* **2013**, *87*, 035423.

[6] Bertolazzi, S.; Brivio, J.; Kis, A. Stretching and breaking of ultrathin MoS_2. *ACS Nano* **2011**, *5*, 9703–9709.

[7] Das, A.; Pisana, S.; Chakraborty, B.; Piscanec, S.; Saha, S. K.; Waghmare, U. V.; Novoselov, K. S.; Krishnamurthy, H. R.; Geim, A. K.; Ferrari, A. C. et al. Monitoring dopants by Raman scattering in an electrochemically top-gated graphene transistor. *Nat. Nanotechnol.* **2008**, *3*, 210–215.

[8] Liang, X. G.; Fu, Z. L.; Chou, S. Y. Graphene transistors fabricated via transfer-printing in device active-areas on large wafer. *Nano Lett.* **2007**, *7*, 3840–3844.

[9] Ovchinnikov, D.; Allain, A.; Huang, Y.-S.; Dumcenco, D.; Kis, A. Electrical transport properties of single-layer WS_2. *ACS Nano* **2014**, *8*, 8174–8181.

[10] Liu, W.; Kang, J. H.; Sarkar, D.; Khatami, Y.; Jena, D.; Banerjee, K. Role of metal contacts in designing high-performance monolayer n-type WSe_2 field effect transistors. *Nano Lett.* **2013**, *13*, 1983–1990.

[11] Castellanos-Gomez, A.; Vicarelli, L.; Prada, E.; Island, J. O.; Narasimha-Acharya, K. L.; Blanter, S. I.; Groenendijk, D. J.; Buscema, M.; Steele, G. A.; Alvarez, J. V. et al. Isolation and characterization of few-layer black phosphorus. *2D Mater.* **2014**, *1*, 025001.

[12] Ling, X.; Wang, H.; Huang, S. X.; Xia, F. N.; Dresselhaus, M. S. The renaissance of black phosphorus. *Proc. Natl. Acad. Sci. USA* **2015**, *112*, 4523–4530.

[13] Xia, F. N.; Wang, H.; Jia, Y. C. Rediscovering black phosphorus as an anisotropic layered material for optoelectronics and electronics. *Nat. Commun.* **2014**, *5*, 4458.

[14] Qiao, J. S.; Kong, X. H.; Hu, Z.-X.; Yang, F.; Ji, W. High-mobility transport anisotropy and linear dichroism in few-layer black phosphorus. *Nat. Commun.* **2014**, *5*, 4475.

[15] Wu, J. X.; Mao, N. N.; Xie, L. M.; Xu, H.; Zhang, J. Identifying the crystalline orientation of black phosphorus using angle-resolved polarized Raman spectroscopy. *Angew. Chem., Int. Ed.* **2015**, *54*, 2366–2369.

[16] Ribeiro, H. B.; Pimenta, M. A.; de Matos, C. J. S.; Moreira, R. L.; Rodin, A. S.; Zapata, J. D.; de Souza, E. A. T.; Castro Neto, A. H. Unusual angular dependence of the Raman response in black phosphorus. *ACS Nano* **2015**, *9*, 4270–4276.

[17] Qin, G. Z.; Yan, Q. B.; Qin, Z. Z.; Yue, S. Y.; Hu, M.; Su, G. Anisotropic intrinsic lattice thermal conductivity of phosphorene from first principles. *Phys. Chem. Chem. Phys.* **2015**, *17*, 4854–4858.

[18] Jain, A.; McGaughey, A. J. H. Strongly anisotropic in-plane thermal transport in single-layer black phosphorene. *Sci. Rep.* **2015**, *5*, 8501.

[19] Fei, R. X.; Yang, L. Lattice vibrational modes and Raman scattering spectra of strained phosphorene. *Appl. Phys. Lett.* **2014**, *105*, 083120.

[20] Hu, T.; Han, Y.; Dong, J. M. Mechanical and electronic properties of monolayer and bilayer phosphorene under uniaxial and isotropic strains. *Nanotechnology* **2014**, *25*, 455703.

[21] Jiang, J. W.; Park, H. S. Negative poisson's ratio in single-layer black phosphorus. *Nat. Commun.* **2014**, *5*, 4727.

[22] Wei, Q.; Peng, X. H. Superior mechanical flexibility of phosphorene and few-layer black phosphorus. *Appl. Phys. Lett.* **2014**, *104*, 251915.

[23] Yu, T.; Ni, Z. H.; Du, C. L.; You, Y. M.; Wang, Y. Y.; Shen, Z. X. Raman mapping investigation of graphene on transparent flexible substrate: The strain effect. *J. Phys. Chem. C* **2008**, *112*, 12602–12605.

[24] Ni, Z. H.; Yu, T.; Lu, Y. H.; Wang, Y. Y.; Feng, Y. P.; Shen, Z. X. Uniaxial strain on graphene: Raman spectroscopy study and band-gap opening. *ACS Nano* **2008**, *2*, 2301–2305.

[25] Mohiuddin, T. M. G.; Lombardo, A.; Nair, R. R.; Bonetti, A.; Savini, G.; Jalil, R.; Bonini, N.; Basko, D. M.; Galiotis, C.; Marzari, N. et al. Uniaxial strain in graphene by Raman spectroscopy: G peak splitting, grüneisen parameters, and sample orientation. *Phys. Rev. B* **2009**, *79*, 205433.

[26] Huang, M. Y.; Yan, H. G.; Chen, C. Y.; Song, D. H.; Heinz, T. F.; Hone, J. Phonon softening and crystallographic orientation of strained graphene studied by Raman spectroscopy. *Proc. Natl. Acad. Sci. USA* **2009**, *106*, 7304–7308.

[27] Pereira, V. M.; Castro Neto, A. H.; Peres, N. M. R. Tight-binding approach to uniaxial strain in graphene. *Phys. Rev. B* **2009**, *80*, 045401.

[28] Kou, L. Z.; Tang, C.; Guo, W. L.; Chen, C. F. Tunable magnetism in strained graphene with topological line defect. *ACS Nano* **2011**, *5*, 1012–1017.

[29] Wang, Y. L.; Cong, C. X.; Qiu, C. Y.; Yu, T. Raman spectroscopy study of lattice vibration and crystallographic orientation of monolayer MoS_2 under uniaxial strain. *Small* **2013**, *9*, 2857–2861.

[30] Wang, Y. L.; Cong, C. X.; Yang, W. H.; Shang, J. Z.; Peimyoo, N.; Chen, Y.; Kang, J.; Wang, J. P.; Huang, W.; Yu, T. Strain-induced direct–indirect bandgap transition and phonon modulation in monolayer WS_2. *Nano Res.* **2015**, *8*, 2562–2572.

[31] Rice, C.; Young, R. J.; Zan, R.; Bangert, U.; Wolverson, D.; Georgiou, T.; Jalil, R.; Novoselov, K. S. Raman-scattering measurements and first-principles calculations of strain-induced phonon shifts in monolayer MoS_2. *Phys. Rev. B* **2013**, *87*, 081307.

[32] He, K. L.; Poole, C.; Mak, K. F.; Shan, J. Experimental demonstration of continuous electronic structure tuning via strain in atomically thin MoS_2. *Nano Lett.* **2013**, *13*, 2931–2936.

[33] Conley, H. J.; Wang, B.; Ziegler, J. I.; Haglund, R. F., Jr.; Pantelides, S. T.; Bolotin, K. I. Bandgap engineering of strained monolayer and bilayer MoS_2. *Nano Lett.* **2013**, *13*, 3626–3630.

[34] Zhang, Q. Y.; Cheng, Y. C.; Gan, L.-Y.; Schwingenschlögl, U. Giant valley drifts in uniaxially strained monolayer MoS_2. *Phys. Rev. B* **2013**, *88*, 245447.

[35] Zhu, C. R.; Wang, G.; Liu, B. L.; Marie, X.; Qiao, X. F.; Zhang, X.; Wu, X. X.; Fan, H.; Tan, P. H.; Amand, T. et al. Strain tuning of optical emission energy and polarization in monolayer and bilayer MoS_2. *Phys. Rev. B* **2013**, *88*, 121301.

[36] Johari, P.; Shenoy, V. B. Tuning the electronic properties of semiconducting transition metal dichalcogenides by applying mechanical strains. *ACS Nano* **2012**, *6*, 5449–5456.

[37] Peng, X. H.; Wei, Q.; Copple, A. Strain-engineered direct–indirect band gap transition and its mechanism in two-dimensional phosphorene. *Phys. Rev. B* **2014**, *90*, 085402.

[38] Fei, R. X.; Yang, L. Strain-engineering the anisotropic electrical conductance of few-layer black phosphorus. *Nano Lett.* **2014**, *14*, 2884–2889.

[39] Li, Y.; Yang, S. X.; Li, J. B. Modulation of the electronic properties of ultrathin black phosphorus by strain and electrical field. *J. Phys. Chem. C* **2014**, *118*, 23970–23976.

[40] Novoselov, K. S.; Jiang, D.; Schedin, F.; Booth, T. J.; Khotkevich, V. V.; Morozov, S. V.; Geim, A. K. Two-dimensional atomic crystals. *Proc. Natl. Acad. Sci. USA* **2005**, *102*, 10451–10453.

[41] Qin, G. Z.; Yan, Q. B.; Qin, Z. Z.; Yue, S. Y.; Cui, H. J.; Zheng, Q. R.; Su, G. Hinge-like structure induced unusual properties of black phosphorus and new strategies to improve the thermoelectric performance. *Sci. Rep.* **2014**, *4*, 6946.

[42] Ling, X.; Liang, L. B.; Huang, S. X.; Puretzky, A. A.; Geohegan, D. B.; Sumpter, B. G.; Kong, J.; Meunier, V.; Dresselhaus, M. S. Low-frequency interlayer breathing modes in few-layer black phosphorus. *Nano Lett.* **2015**, *15*, 4080–4088.

[43] Sugai, S.; Shirotani, I. Raman and infrared reflection spectroscopy in black phosphorus. *Solid State Commun.* **1985**, *53*, 753–755.

[44] Ferrari, A. C.; Meyer, J. C.; Scardaci, V.; Casiraghi, C.; Lazzeri, M.; Mauri, F.; Piscanec, S.; Jiang, D.; Novoselov, K. S.; Roth, S. et al. Raman spectrum of graphene and graphene layers. *Phys. Rev. Lett.* **2006**, *97*, 187401.

[45] Lee, C.; Yan, H. G.; Brus, L. E.; Heinz, T. F.; Hone, J.; Ryu, S. Anomalous lattice vibrations of single- and few-layer MoS_2. *ACS Nano* **2010**, *4*, 2695–2700.

[46] Li, S.-L.; Miyazaki, H.; Song, H. S.; Kuramochi, H.; Nakaharai, S.; Tsukagoshi, K. Quantitative Raman spectrum and reliable thickness identification for atomic layers on insulating substrates. *ACS Nano* **2012**, *6*, 7381–7388.

[47] Late, D. J.; Liu, B.; Matte, H. S. S. R.; Rao, C. N. R.; Dravid, V. P. Rapid characterization of ultrathin layers of chalcogenides on SiO_2/Si substrates. *Adv. Funct. Mater.* **2012**, *22*, 1894–1905.

[48] Cong, C. X.; Yu, T.; Saito, R.; Dresselhaus, G. F.; Dresselhaus, M. S. Second-order overtone and combination Raman modes of graphene layers in the range of 1690−2150 cm^{-1}. *ACS Nano* **2011**, *5*, 1600–1605.

[49] Cong, C. X.; Yu, T.; Sato, K.; Shang, J. Z.; Saito, R.; Dresselhaus, G. F.; Dresselhaus, M. S. Raman characterization of ABA- and ABC-stacked trilayer graphene. *ACS Nano* **2011**, *5*, 8760–8768.

[50] Voiry, D.; Yamaguchi, H.; Li, J. W.; Silva, R.; Alves, D. C. B.; Fujita, T.; Chen, M. W.; Asefa, T.; Shenoy, V. B.; Eda, G. et al. Enhanced catalytic activity in strained chemically exfoliated WS_2 nanosheets for hydrogen evolution. *Nat. Mater.* **2013**, *12*, 850–855.

[51] Ni, Z. H.; Liu, L.; Wang, Y. Y.; Zheng, Z.; Li, L.-J.; Yu, T.; Shen, Z. X. G-band Raman double resonance in twisted bilayer graphene: Evidence of band splitting and folding. *Phys. Rev. B* **2009**, *80*, 125404.

[52] Casiraghi, C.; Hartschuh, A.; Qian, H.; Piscanec, S.; Georgi, C.; Fasoli, A.; Novoselov, K. S.; Basko, D. M.; Ferrari, A. C. Raman spectroscopy of graphene edges. *Nano Lett.* **2009**, *9*, 1433–1441.

[53] Cong, C. X.; Yu, T.; Wang, H. M. Raman study on the G mode of graphene for determination of edge orientation. *ACS Nano* **2010**, *4*, 3175–3180.

[54] You, Y. M.; Ni, Z. H.; Yu, T.; Shen, Z. X. Edge chirality determination of graphene by Raman spectroscopy. *Appl. Phys. Lett.* **2008**, *93*, 163112.

[55] Wang, Y. Y.; Ni, Z. H.; Liu, L.; Liu, Y. H.; Cong, C. X.; Yu, T.; Wang, X. J.; Shen, D. Z.; Shen, Z. X. Stacking-dependent optical conductivity of bilayer graphene. *ACS Nano* **2010**, *4*, 4074–4080.

[56] Peimyoo, N.; Shang, J. Z.; Yang, W. H.; Wang, Y. L.; Cong, C. X.; Yu, T. Thermal conductivity determination of suspended mono- and bilayer WS_2 by Raman spectroscopy. *Nano Res.* **2015**, *8*, 1210–1221.

[57] Li, H.; Lu, G.; Wang, Y. L.; Yin, Z. Y.; Cong, C. X.; He, Q. Y.; Wang, L.; Ding, F.; Yu, T.; Zhang, H. Mechanical exfoliation and characterization of single- and few-layer nanosheets of WSe_2, TaS_2, and $TaSe_2$. *Small* **2013**, *9*, 1974–1981.

[58] Late, D. J.; Shirodkar, S. N.; Waghmare, U. V.; Dravid, V. P.; Rao, C. N. R. Thermal expansion, anharmonicity and temperature-dependent Raman spectra of single- and few-layer $MoSe_2$ and WSe_2. *Chemphyschem* **2014**, *15*, 1592–1598.

[59] Late, D. J.; Maitra, U.; Panchakarla, L. S.; Waghmare, U. V.; Rao, C. N. R. Temperature effects on the Raman spectra of graphenes: Dependence on the number of layers and doping. *J. Phys.: Condens. Mat.* **2011**, *23*, 055303.

[60] Nagaleekar, T. M.; Late, D. J. Temperature dependent phonon shifts in single-layer WS_2. *ACS Appl. Mater. Interfaces* **2014**, *6*, 1158–1163.

[61] Zhang, S.; Yang, J.; Xu, R. J.; Wang, F.; Li, W. F.; Ghufran, M.; Zhang, Y.-W.; Yu, Z. F.; Zhang, G.; Qin, Q. H. et al. Extraordinary photoluminescence and strong temperature/ angle-dependent Raman responses in few-layer phosphorene. *ACS Nano* **2014**, *8*, 9590–9596.

[62] Castellanos-Gomez, A.; Vicarelli, L.; Prada, E.; Island, J. O.; Narasimha-Acharya, K. L.; Blanter, S. I.; Groenendijk, D. J.; Buscema, M.; Steele, G. A.; Alvarez, J. V. et al. Isolation and characterization of few-layer black phosphorus. *2D Mater.* **2014**, *1*, 025001.

[63] Liu, H.; Neal, A. T.; Zhu, Z.; Luo, Z.; Xu, X. F.; Tománek, D.; Ye, P. D. Phosphorene: An unexplored 2D semiconductor with a high hole mobility. *ACS Nano* **2014**, *8*, 4033–4041.

[64] Lu, W. L.; Nan, H. Y.; Hong, J. H.; Chen, Y. M.; Zhu, C.; Liang, Z.; Ma, X. Y.; Ni, Z. H.; Jin, C. H.; Zhang, Z. Plasma-assisted fabrication of monolayer phosphorene and its Raman characterization. *Nano Res.* **2014**, *7*, 853–859.

[65] Late, D. J. Temperature dependent phonon shifts in few-layer black phosphorus. *ACS Appl. Mater. Interfaces* **2015**, *7*, 5857–5862.